Quantitative Signal Analysis of Sum-Frequency Scattering Experiments from Aerosol Surfaces

Jesse B. Brown, Yuqin Qian, Hui Wang, Tong Zhang, Zhi-Chao Huang-Fu, and Yi Rao*

Department of Chemistry and Biochemistry, Utah State University, Logan, UT 84322

Abstract

Interfaces are instrumental in processes of biology, engineering, production, and environmental systems. The chemical and physical properties of heterogeneous interfaces are known to be different from those of their underlying bulk phases, and different again when considering the curved surface of submicron aerosol droplets. The recently-developed technique of vibrational sum-frequency scattering (VSFS) spectroscopy from airborne particles has emerged as an interface-specific method for the *in-situ* analysis of this unique system. While the technique has shown promise in debut works, a quantitative analysis of the VSFS system has not yet been performed. Here we provide a comprehensive analysis of a VSFS spectrometer with reference to the well-documented planar analog. We decompose the VSFS signal into coherent and incoherent as well as resonant and nonresonant components as a function of incident pulse delay time. We also quantify and compare resonant and nonresonant VSFS and VSFG experimental data using the same laser and detection systems. Using the air/water interface as a guide, we show that the resonant and nonresonant contributions to the SF responses are comparable for the two systems by extracting second-order susceptibilities and hyperpolarizabilities and using them to estimate single-particle susceptibilities. A quantitative analysis of the signal detection systems for the scattering and planar geometries is made, and conversion efficiencies for VSFG, VSFS, and other nonlinear scattering experiments are compared. Lastly, the possibility of a low-repetition (1 kHz) VSFS spectrometer is considered, determining that it may be possible with modern laser technology but is inevitably less efficient than a high-repetition (100 kHz) system. Though this multistep analysis we obtain a better understanding of the components of the VSFS signal from aerosol particles, further validate the feasibility of the experiments, and provide insight to those wishing to conduct similar experiments and how they may be improved.

Introduction

Surfaces and interfaces are chemically and physically unique due to their inherent breakage of symmetry. The importance of interfaces to chemistry and physics cannot be understated, as they are the point of entry for any contact or interaction with a system or material. As such, the surfaces of small-volume systems such as nanodroplets and aerosol particles becomes increasingly important with decreased size due to their high surface area to volume ratio. With these unique surface properties, droplets and particle surfaces have been researched with focusses on catalysis, synthesis, and the atmospheric processes of aerosol particles. For example, the oxidation of alcohols using the two-phase system of microdroplets and a sheath gas has been demonstrated without the need for additional catalysts.[1] Adjacently, humidified acid-base microreactors have been used to synthesize lithium vanadate particles for battery applications.[2] More recently, ribonucleotide synthesis was demonstrated in the system of aqueous reactants sprayed into the air, with the reaction likely proceeding near the micrometer-sized droplet surface.[3] Small droplets and particles also have atmospheric relevance due to the ubiquity and abundance of aerosols.[4, 5] In such systems, surface reactions directly contribute to the growth and multiplication of aerosol particles. These heterogenous surface reactions can lead to volatile products which desorb from the particle surface and can then undergo photochemical and gas phase reactions to form new aerosols.[6-9] Meanwhile, less volatile products can be taken into the particle bulk where they affect the particle properties such as pH and refractive.[10, 11] While in the interior of the particle, these compounds can undergo further reactions which may produce new surface-active species and complete the cycle.[12, 13] Due to their important and unique surface properties, analytical techniques witch surface specificity are ideal to study these systems. Nonlinear optical techniques like

second-harmonic and sum-frequency generation (SHG and SFG, respectively) spectroscopies are inherently sensitive to interfaces and surfaces, making them ideal high surface area systems.[5, 14]

In SFG spectroscopy, two laser pulses, one visible and the other in the IR, are incident on a sample at the same point in time and space and produce a signal whose frequency is the sum of the two incident frequencies. In such a process, the IR pulse is resonant with a vibrational mode of the irradiated sample, resulting in VSFG. Like SFG, second-harmonic generation (SHG) occurs when the two incident pulses have the same frequency. VSFG spectroscopy is an interface-specific nonlinear optical spectroscopic technique that grew in popularity in the 1980's.[15, 16] In 1996, the Eisenthal group demonstrated second harmonic scattering (SHS) from the surface of micron-sized polystyrene spheres coated in an SH-active dye suspended in water.[17] Only six years later, VSFS was shown to be applicable to an emulsion of hexadecane in water, and theoretical considerations allowed the calculation of molecular orientation of the droplet/water interface.[18] Around the same time, diffuse reflectance SFG from powder surfaces, another breakthrough form of SFS.[19] These ~~two~~ milestones in nonlinear optics led to fruitful applications of SHS[20-22] and SFS[23-25] in fields from colloidal to biological systems. Recently, these SHS and SFS have been extended to aerosol systems, where their unique surface specificity is of paramount importance.[26-32] While the importance of such nonlinear scattering results to aerosol and surface science has been discussed already,[14] the technique—specifically VSFS—and its implementation is still in its infancy. In fact, the validity of the VSFS signal as it has been demonstrated from submicron aerosols with high dilution (~10^6 cm^{-3}) was called into question in 2023, suggesting that the observed signal was 10^7 more intense than what could be experimentally observed according to the current nonlinear scattering theories.[33] Even through these concerns were shown to be inaccurate,[34] a technical analysis from a tutorial perspective of VSFS has not yet been provided.

In the implementation of VSFS from aerosol particles, the fundamental principles from the well-established techniques of planar VSFG and VSFS from emulsions still apply. This leaves only experimental differences to be the root cause of the weak observed signal, i.e., the traditional systems of VSFG and VSFS are static and geometrically different from the emerging technique of VSFS from a flow of airborne particles. Herein, we provide a quantitative analysis of both nonresonant and resonant VSFS responses from streams of aerosol particles and use the planar liquid surface as a reference point by which to understand the VSFS signals, with the aim of finding a common ground on which to base our experiments. To do this, we analyze the VSFS signal at different time delays between the incident pulses to extract the relative resonant and nonresonant contributions to the signal. By comparing the resonant and nonresonant responses from VSFS and VSFG experiments using the same laser and detection systems, we quantitatively compare corresponding systems. We then use the VSFG response from the air/liquid interface to extract second-order susceptibilities and hyperpolarizabilities for resonant and nonresonant systems which are then used to estimate aerosol susceptibilities and compare them to the experimental results. Furthermore, a robust analysis of the presented VSFS and VSFG spectrometers is provided, along with quantitative comparison of detection efficiencies for planar and aerosol systems. Lastly, we discuss and provide our opinion on the possibility of conducting aerosol VSFS experiments using a commercially common 1 kHz 800 nm laser system.

Experimental Section

VSFS and VSFG Experiments

Both VSFS and VSFG experiments at 100 kHz repetition rate used the same laser and detection systems, which were the same as those previously reported for VSFS.[27-29, 34] The laser used was a Pharos femtosecond pulsed integrated laser/amplifier (Light Conversion) with an output of 10.0 W at 100 kHz and a central wavelength of 1030 nm. This was used to pump an optical parametric amplifier (OPA) which produced a tunable IR pulse from 1500 to 4500 nm (Orpheus-ONE, Light Conversion). The detector system used consisted of a spectrometer (Acton 300i, Princeton Instruments) with a 1200-blaze grating, fitted with a

liquid N_2-cooled charge coupled device (CCD) detector (LN/CCD-1340/400, Princeton Instruments). Spectral data were then collected using WinSpec software (Princeton Instruments). For convenience, key experimental parameters for VSFS and VSFG experiments are summarized in Table S1. The details for VSFG experiments at 1 kHz and 100 kHz can be found in the SI.

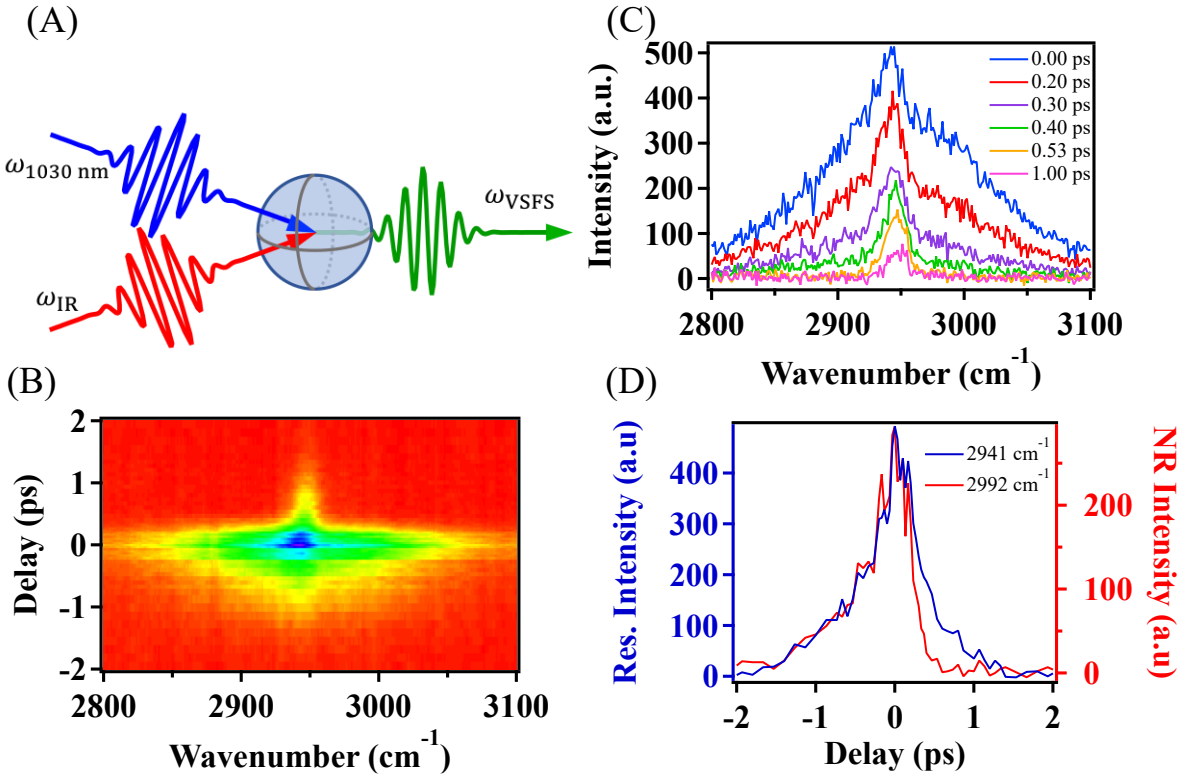

Figure 1. (A) 1030 nm and IR pulses incident on a spherical aerosol particle generating scattered SFS signal 0° relative to the incident 1030 nm pulse. (B) 2D pseudo-color plot of VSFS spectra of 6 M acetonitrile in 0.5 M NaCl at different time delays between the 1030 nm and IR Pulse (positive time defines 1030 nm pulse arriving after the IR pulse. (C) VSFS spectra extracted from 2D plot at -0.75 to 0.00 ps delays. (D) Time traces extracted from 2D plot highlighting resonant and nonresonant peaks.

VSFS at 100 kHz. In the VSFS experiments, the residual 1030 nm pulse from the OPA was first directed to an air-spaced etalon (SLS Optics), followed by a halfwave plate (Thorlabs, WPH10M-1030), and a translation stage, which controlled the pulse duration, incident polarization, and temporal delay, respectively. The 1030 nm pulse was then directed and focused (f=25.0 cm) on the stream of aerosol particles, and its propagation direction defined the x-axis of the experimental geometry. The IR pulse passed through a halfwave plate (Thorlabs, WPLH05M-3500) after exiting the OPA and was then directed to and focused (f=10.0 cm) on the stream of aerosol particles with an incident angle of ~5° with respect to the x-axis. Such a geometry results in an incident plane which is parallel to the optical table and lies within the xy-plane. The spot sizes of the 1030 and IR beams measured in the center of the aerosol streams are shown in Table S1, and their exact focal points were located slightly after the sample to further prevent SFG from optics surfaces. The focal points were located as near as possible to each other to maximize signal intensity. A 2"-diameter collecting lens (f=3.2 cm) was oriented 0° relative to x-axis, which collected a 60° portion of the scattered SF signal from the aerosol particles. To prevent damage to the detection system, it was necessary to block the forward propagation of the 1030 nm pulse after the sample. This was achieved using a small screw suspended near the collection lens which blocked the focused laser as well as approximately

5° of the VSFS signal. The signal was then directed through a thin-film analyzer (Thorlabs) before being focused by another lens onto the entrance slit of the spectrometer. The polarizations of the incident and detected lights in VSFS experiments are defined with respect to the optical table: H-polarization is horizontal and is parallel to the table, while V-polarization is vertically oriented and is perpendicular to the optical table. The polarization of the three beams is listed in order of increasing wavelength, as is conventional. All VSFS experiments were conducted using a forward-propagating geometry which provides a signal intensity ~7x stronger than the previously-published 90º collection experiments.[14, 27-29, 34] A quantitative analysis of the angle-dependent VSFS signal intensity from aerosols cannot currently be obtained due to the weak signal and the lack of a reference material, such as hyper-Rayleigh scattering used in liquid SFS experiments.[35]

Aerosol Generation

Aerosol particles were generated with a constant flow aerosol generator (3076, TSI) using 4.0 slpm N_2 gas and drawing from a stock solution of aqueous 0.5 M NaCl. This produced a stream of aerosol particles with a density, N_p, of 3.9×10^7 cm^{-3}, with a lognormal size distribution and a mean particle diameter of 100 nm, as shown in Figure S10 in the SI. The stream of aerosol particles passed through a 1-meter PTFE tube with 1/4" OD that was connected to the aerosol chamber. Aerosols were eluted into the overlapped 1030 nm and IR beams using a glass tube with 4 mm ID. A catch vessel attached to a vacuum pump was used to extract aerosols from the chamber and optics were inspected routinely to ensure no accumulation of aerosols. NaCl was purchased from Fisher Chemical and baked at 600 °C overnight before use. Acetonitrile (99.9%) was purchased from Fisher Chemical and used as received. Solutions of 6.0 M acetonitrile were prepared in 0.5 M NaCl, and the same solutions were used for all experiments.

The detection efficiency of the planar VSFG experiments was normalized using a left-handed quartz crystal,[36-38] and both VSFS and VSFG experiments used the same spectrometer and CCD. The antireflective coating on the lenses used in both experiments resulted in minimal signal intensity loss from reflections. The system of a stream aerosol particles in air has no background contributions from the sample nor from room light. The background-free system in combination with the selected CCD results in a system that is shot-noise limited due to the very low dark current noise afforded by the liquid N_2-cooled detector.

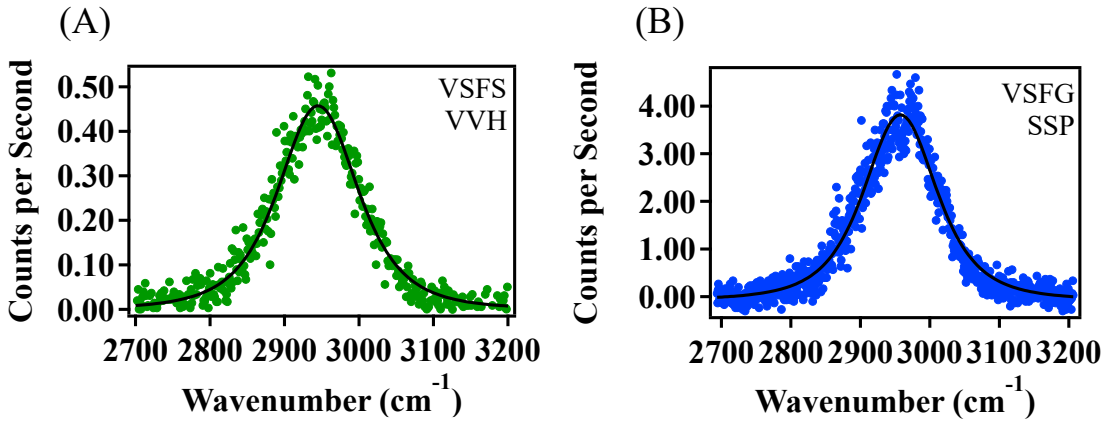

Figure 2. Nonresonant VSF spectra of (A) aerosol particles generated from 0.5 M NaCl solution under VVH polarization; and (B) planar surface under SSP polarization of 0.5 M NaCl solution at 100 kHz laser repetition. Counts per second refers to intensity counts after ADC by the detector, not photons per second.

Results

When conducting VSF experiments, researchers have to deal with both resonant and nonresonant responses from the material, usually detuning the temporal overlap between the incident pulse to suppress the nonresonant background and easily extract the desired resonant information.[39-42] We found that our VSFS experiments form aqueous droplets have very strong nonresonant background, as shown in the enveloping peak in Figures 1. Shown in the representative spectra in Figure 1(C), the system of 6.0 M CH_3CN in aqueous 0.5 M NaCl results in a broad peak from about 2800 to 3100 cm^{-1} and a sharp peak at 2940 cm^{-1}. The sharp peak was attributed to the resonant VSFS from CH_3CN,[43, 44] while the broad feature is nonresonant VSFS. These assignments are further corroborated by the broad envelope decreasing faster with increased time delay that the CH_3CN peak, which persists with the free inductive decay of the resonance,[41, 42] shown explicitly in Figure 1(D). As discussed in detail in the SI, fitting the VSFS data to an incoherent SFG function shown in Figures S1 and S2 showed that the large nonresonant envelope was in fact incoherent sum-frequency scattering (*i*SFS), separate from the other nonresonant contributions. Such an *i*SFS signal reflects the shape of the incident IR pulse, as is seen from metal surfaces in planar VSFG experiments. From this analysis we were able to find that without the *i*SFS response, the resonant-to-nonresonant ration, $\left|\chi^{(2)}_{R,VSFS}\right| : \left|\chi^{(2)}_{NR,VSFS}\right|$, is about 3.95:1. This is an important metric for quantitatively comparing VSFS and VSFG responses below. For comparison to the time-delay data from VSFS experiments shown in Figure 1, delay scanning experiments are shown for nonresonant VSFS and VSFG systems in Figures S3 and S4, respectively. Due to the large *i*SFS contribution, our resonant VSFS experiments were conducted with a delay of 400 fs while nonresonant VSFS experiments were conducted with a delay of 0.0 ps. Resonant and nonresonant planar VSFG experiments were conducted with a delay of 0.0 ps due to minimal nonresonant contribution and to retain maximum signal intensity.

Our analysis of the VSFS response continues by comparing the nonresonant SF responses from aerosol particles and planar surfaces for the same solution of 0.5 M NaCl solution. The nonresonant VSFS and VSFG responses from the 0.5 M aqueous NaCl solution are shown in Figures 2 (A) and (B). These VSF results are nonresonant, meaning that none of the involved beams, ω_{SF}, ω_1, or ω_2, are resonant with a vibrational or electronic mode of the system. Such nonresonant spectra result in broad, gaussian-like peaks centered at ω_{SF}. For the VSFS spectrum in Figure 2 (A), an acquisition time of 60 s with 2x hardware binning were used and have been accounted for in the displayed spectrum whose *y*-axis is in counts per second (CPS) for ease of comparison. Here, the observed counts per second are not to be confused with photons, as this is after the analog-to-digital conversion (ADC). Here, we see that the nonresonant response from the aerosol droplets was about 0.5 CPS. On the other hand, the nonresonant VSFG spectrum in Figure 2 (B) resulted in an intensity of about 4 CPS, suggesting that the signal from the aerosols is about 8-times weaker. These two spectra are displayed in the correlated VVH and SSP polarization combinations because it gives the most intense response from the planar surface. VSFS spectra in VHV, HVV, and HHH polarization combinations are shown in Figure S3. For this nonresonant experiment, the most intense VSFS response was obtained under the HHH polarization combination, followed by the VHV, HVV, and VVH polarizations. The time delay data for nonresonant VSFS from aqueous droplets can also tell us about the origins of the response. As shown in Figure S3 (D), the time traces at the nonresonant wavenumbers from CH_3CN and aqueous systems are very similar after intensity normalization. As this feature in the resonant

case described above was attributed to *i*SFS, we further assert that the VSFS spectrum in Figure 2(A) is largely dominated by incoherent contributions.

Resonant spectra were also collected from three VSF systems to better understand the relationship between the resonant and non-resonant scattered vibrational SF signals from aerosol particles. To do this, high-repetition VSFS and VSFG spectra as well as low-repetition VSFG spectra were collected using 6.0 M acetonitrile in 0.5 M NaCl. All three spectra shown in Figure 3 show one clear peak at 2937 cm^{-1}, which

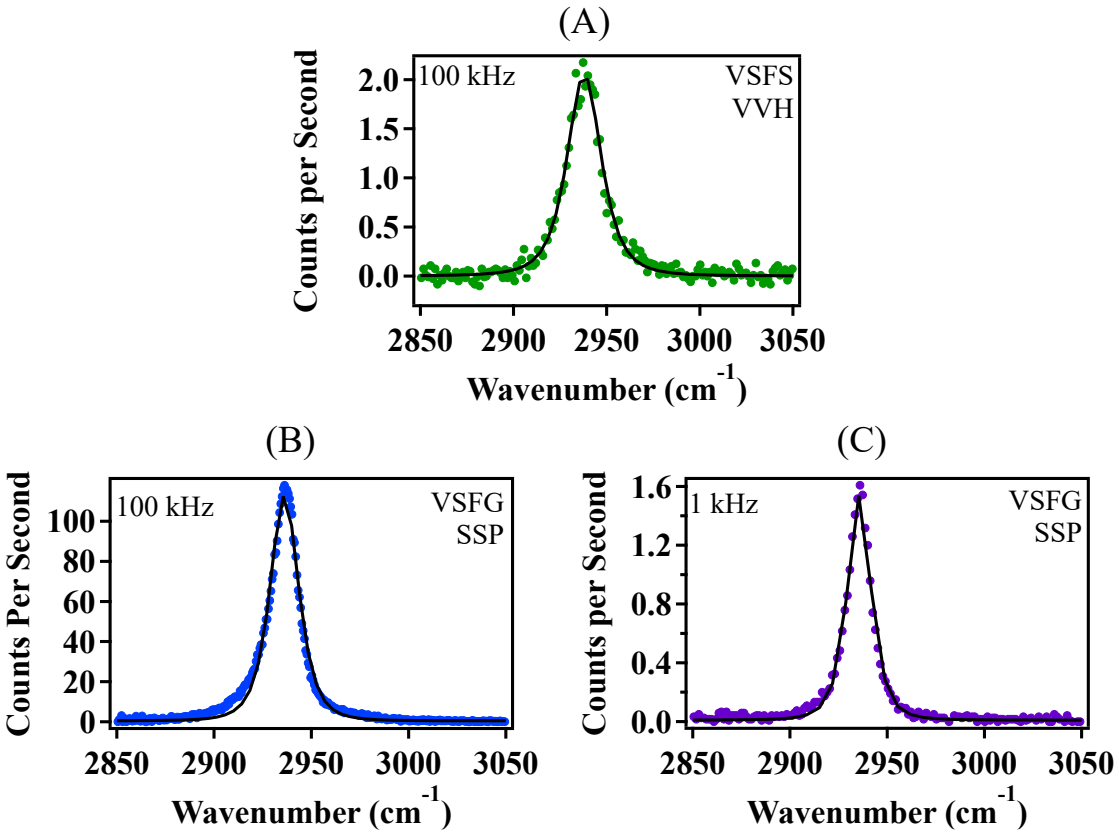

Figure 3. Resonant VSF spectra of (A) aerosol particles generated from 6.0 M acetonitrile in 0.5 M NaCl solution (B) planar surface of 6.0 M acetonitrile in 0.5 M NaCl solution at 100 kHz laser repetition, and (C) planar surface of 6.0 M acetonitrile in 0.5 M NaCl solution at 1 kHz laser repetition. Counts per second refers to intensity counts after ADC by the detector, not photons per second.

is denoted as the -CH_3 symmetric stretching mode.[43] These three spectra have also been modified to display intensity in terms of CPS. The VSFS spectrum of acetonitrile-containing aerosols shown in Figure 3 (A) resulted in a peak intensity of about 2.0 CPS, using an acquisition of 60 s with 2x hardware binning. On the other hand, the VSFG spectrum from the surface of the same solution, shown in Figure 3 (B), resulted in a peak intensity of nearly 120 CPS using just 30 s of acquisition with no binning, 60x more intense than its aerosol counterpart. A VSFG spectrum of the acetonitrile solution surface was also collected using a 1 kHz repetition rate laser system, as shown in Figure 3 (C). This resulted in a peak intensity of only 1.6 CPS, even weaker than that observed from the aerosol surface. As with the nonresonant spectra, these spectra are displayed in the SSP (VVH) polarization combination, as it gives the most intense response from the planar solution surface. We found yet again that the HHH polarization combination gives the most intense response for the VSFS experiments, as shown in Figure S4. For the resonant VSFS experiments, the other polarization gave a weaker response in the following order: VHV, VVH, and HVV.

Discussion

Sum-frequency spectroscopies provide characterization of molecules at surfaces and interfaces by a second-order nonlinear optical process where the SF signal, ω_{SF}, whose frequency is the sum of the two incident frequencies: $\omega_{\mathrm{SF}} = \omega_1 + \omega_2$. In SFG experiments, the response of the material is given by its second order susceptibility, $\chi^{(2)}$, which is a function of the molecular system's hyperpolarizability, $\beta^{(2)}$.[14, 15, 45-47] This direct relationship between the observed response and the interfacial molecular system allows for the normalization of experimental data to account for experimental differences such as laser properties, experimental geometry, etc. This is often done using reference materials such as quartz and gold.[36, 38, 48, 49] However, no such standard materials have been implemented in airborne SFS experiments. For this reason, we built custom SFG and SFS spectrometers which use the same incident laser and signal collection systems to quantitatively compare the two experiments and to search for a general reference for SFS systems. Specifically, we will use the SFG responses from the air/liquid interface, normalized by a z-cut α-quartz crystal, to quantify the associated $\chi^{(2)}$ and $\beta^{(2)}$ values, and use this hyperpolarizability to determine the $\chi^{(2)}$ from an airborne droplet of a given size to better understand the origins of our observed SFS signals.

Extraction of Hyperpolarizabilities of Resonant -CH_3 and Nonresonant H_2O from VSFG Measurements of the Planar Air/Water Interface

The observed signal intensity from SFG experiments, $\gamma_{\mathrm{SF}}(\omega)$, can be described as follows:[45, 50, 51]

$$\gamma_{\mathrm{SF}}(\omega) = \frac{4\pi^2 \omega_{\mathrm{SF}} \sec^2\beta}{\hbar \epsilon_0 c^3 n(\omega_{\mathrm{SF}}) n(\omega_{\mathrm{vis}}) n(\omega_{\mathrm{IR}})} \left|\chi^{(2)}_{eff,i}\right|^2 I(\omega_{\mathrm{vis}}) I(\omega_{\mathrm{IR}}) A(\omega_{\mathrm{IR}})\, \tau_i R D \qquad \text{Eq. 1}$$

where ω_i (s^{-1}) are the frequencies of the generated and incident lights, β is the angle of incidence, $\hbar$ (J s)is the reduced Planck's constant, ε_0 (C $m^{-1}V^{-1}$) is the permittivity of free space, c (m s^{-1}) is the speed of light, $n(\omega_i)$ are the refractive indices of the individual beams at the interface, and $\chi^{(2)}_{eff}$ (m^2 V^{-1}) is the effective second-order susceptibility of the material. $I(\omega_i)$ (W m^{-2})$= E(\omega_i)/\tau_i A(\omega_i)$ are the intensities of the incident beams where $E(\omega_i)$ (J) is the energy, τ_i (s) is the pulse duration, $A(\omega_i)$ (m^2) is the area of the focal spot on the sample, and R (s^{-1}) is the laser repetition rate. Lastly, D is a normalization factor which accounts for the efficiency of the detection system. For the reader's convenience, a detailed discussion of the efficiency of nonlinear optical spectrometers can be found in the SI. The susceptibility term describes the macroscopic response of a material which contributes to the surface-specific SF signal and is a known value for various materials; nonlinear and otherwise.

The effective second-order susceptibility for left-handed quartz crystals, $\chi^{(2)}_q$ of 8.0×10^{-13} m V^{-1} was adopted for an experimental standard in our case.[36, 37] The SSP polarized $\chi^{(2)}_{eff,\mathrm{Q}}$ can then be determined using the following relationships:[37]

$$\left|\chi^{(2)}_{eff,Q}\right| = g\cos\beta_{\mathrm{IR}} L_{yy,\mathrm{SF}} L_{yy,\mathrm{Vis}} L_{xx,\mathrm{IR}} \chi^{(2)}_q l_c = 1.65 \times 10^{-20}\ \frac{\mathrm{m}^2}{\mathrm{V}} \qquad \text{Eq. 2}$$

where g is a proportionality constant, β_i is the incident angle of the IR pulse with respect to the surface normal, and $L_{i,j}$ are the Fresnel factors associated with the incident and generated beams (see SI, Eqs. S3 and Table S3), and l_c is the coherence length of the SF signal in a given medium.[37] In our experiments, l_c values of 53.7 nm and 60.9 nm were calculated using Eq. S2 for the z-cut left-handed α-quartz and aqueous surfaces, respectively. Once the polarization-dependent $\chi^{(2)}_{eff,\mathrm{Q}}$ values are known, the following expression was used to determine the effective susceptibility for a given experimental system:

$$\left|\chi^{(2)}_{eff,i}\right| = \sqrt{\frac{\left(\frac{I_{\mathrm{VSFG},i}}{J_{\mathrm{VSFG},i}}\right)}{\left(\frac{I_{\mathrm{VSFG,Q}}}{J_{\mathrm{VSFG,Q}}}\right)}\left|\chi^{(2)}_{eff,\mathrm{Q}}\right|^2}. \quad \text{Eq. 3}$$

In this expression, $J_{\mathrm{VSFG},i} = I(\omega_{\mathrm{vis}})I(\omega_{\mathrm{IR}})A(\omega_{\mathrm{IR}})T\,R$, where T is the experimental acquisition time. $I_{\mathrm{VSFG},i}$ are the experimental resonant and nonresonant VSFG spectra in Figures 2(B) and 3(B). $I_{\mathrm{VSFG,Q}}$ is the experimental SFG intensity of the z-cut α-quartz shown in Figure S7. The resultant normalized $\left|\chi^{(2)}_{eff,i}\right|$ spectra are shown in figures S8 and S9 for the susceptibilities of the nonresonant response of the 0.5 M NaCl surface and the resonant response of the 6.0 M CH_3CN surface, respectively. It is shown that the $\left|\chi^{(2)}_{eff,\mathrm{H_2O}}\right|$, the response of the aqueous 0.5 M NaCl surface, is nearly constant with a value around 3.22×10^{-22} $\mathrm{m^2V^{-1}}$ at 2937 $\mathrm{cm^{-1}}$. The nonresonant susceptibility is constant because the nonresonant peaks from quartz and the 0.5 M NaCl surface both represent the shape of the incident IR pulse intensity. As shown in Figure S9, $\left|\chi^{(2)}_{eff,-\mathrm{CH_3}}\right|$ retains the peak shape from the experiments and can be fitted using the following equation:

$$\left|\chi^{(2)}_{eff,-\mathrm{CH_3}}\right| = \left|\chi^{(2)}_{NR} + \frac{A^{(2)}_{eff,-\mathrm{CH_3}}}{2\pi c\left(\omega - \omega_{-\mathrm{CH_3}} + i\Gamma_{-\mathrm{CH_3}}\right)}\right|. \quad \text{Eq. 4}$$

Here, $A^{(2)}_i$ $(\mathrm{m^2V^{-1}s^{-1}})$ is the strength factor, ω_i $(\mathrm{cm^{-1}})$ is the central frequency of the ith vibrational mode, and Γ_i $(\mathrm{cm^{-1}})$ is a damping constant, where a factor of $2\pi c$ from the original unit of $\mathrm{cm^{-1}}$ results in the final units of the strength factor. Curve fitting of the $\left|\chi^{(2)}_{eff,-\mathrm{CH_3}}\right|$ spectrum in Figure S9 results in a value of $\Gamma_{-\mathrm{CH_3}}$ =6.21 ± 0.44 $\mathrm{cm^{-1}}$. At the peak intensity at 2937.0 $\mathrm{cm^{-1}}$, the resonant contribution to $\left|\chi^{(2)}_{eff,\ R,-\mathrm{CH_3}}\right| = \left|A^{(2)}_{eff,-\mathrm{CH_3}}/2\pi c\Gamma_{-\mathrm{CH_3}}\right| = 1.03 \times 10^{-21}\ \mathrm{m^2\,V^{-1}}$. Here we find that the ratio of the resonant and nonresonant effective susceptibilities is about 3.2:1. Additionally, these spectral fitting parameters can be found in Table S4 in the Supporting Information. Similarly, for the nonresonant response from the air/water interface, there is no resonant contribution, but it can still be expressed in the form

$$\left|\chi^{(2)}_{eff,\mathrm{H_2O}}\right| = \left|\chi^{(2)}_{eff,\mathrm{H_2O},NR}\right| = \left|\frac{A^{(2)}_{eff,\mathrm{H_2O},NR}}{2\pi c\left(\omega - \omega_{\mathrm{H_2O}} + i\Gamma_{\mathrm{H_2O}}\right)}\right|. \quad \text{Eq. 5}$$

Here, $\Gamma_{\mathrm{H_2O}} = 0$, because there is no resonance with water molecules at the probed frequency. The nearest resonance of water is assumed to be near 3400 $\mathrm{cm^{-1}}$,[52] so we get that $\Delta\omega = \left|\omega - \omega_{\mathrm{H_2O}}\right| = 450\ \mathrm{cm^{-1}}$ and can simply state that $\left|\chi^{(2)}_{eff,\mathrm{H_2O},NR}\right| = \left|A^{(2)}_{eff,\mathrm{H_2O},NR}/2\pi c\Delta\omega\right| = 3.22 \times 10^{-22}$ $\mathrm{m^2V^{-1}}$ at 2937 $\mathrm{cm^{-1}}$.

Next, we must consider that due to the large size of the IR spot size on the sample compared to the molecules, not all irradiated molecules will oscillate coherently but in many discrete coherent domains. As such, the SF intensity is directly proportional to the number of coherent domains being irradiated, N_{coh}. Coherent domains are irradiated zones in which the oscillations that generate the SF signal are in phase with each other. For both resonant and nonresonant SF responses, the coherent domains do not propagate with very long distance. For our calculations, they were assumed to have a diameter equal to l_c. Accordingly, $\left|\chi^{(2)}_{eff,i}\right| = \left|\chi^{(2)}_{eff,i,coh}\right|\sqrt{N_{coh}}$ with $N_{coh} = 2.24 \times 10^6$. This consideration then gives that $\left|\chi^{(2)}_{eff,\ R,-\mathrm{CH_3},coh}\right| = 6.91 \times 10^{-25}\ \mathrm{m^2V^{-1}}$. Likewise, $\left|\chi^{(2)}_{eff,NR,\mathrm{H_2O},coh}\right| = 2.15 \times 10^{-25}\ \mathrm{m^2V^{-1}}$.

To obtain hyperpolarizabilities for $-CH_3$ and H_2O, we must account for local field factors to determine $\left|\chi^{(2)}_{R,-CH_3,coh}\right|$ from $\left|\chi^{(2)}_{eff,R,-CH_3,coh}\right|$ and $\left|\chi^{(2)}_{NR,H_2O,coh}\right|$ from $\left|\chi^{(2)}_{eff,NR,H_2O,coh}\right|$. Since our SFG signal comes primarily from the monolayer at the air/liquid interface, we modify Eq. 2 to the form of

$$\left|\chi^{(2)}_{i,coh}\right| = \frac{\left|\chi^{(2)}_{eff,i,coh}\right|}{cos\,\beta_{IR} L_{yy,SF} L_{yy,Vis} L_{zz,IR}}, \quad \text{Eq. 6}$$

resulting in $\left|\chi^{(2)}_{R,-CH_3,coh}\right| = 4.86 \times 10^{-24}\ m^2V^{-1}$ and $\left|\chi^{(2)}_{NR,H_2O,coh}\right| = 1.51 \times 10^{-24}\ m^2V^{-1}$.

Ultimately, the macroscopic response of the material is the sum of all the molecular-level responses and can be expressed as

$$\chi^{(2)}_{i,coh} = n_{i,\,coh}\langle\beta^{(2)}_i\rangle, \quad \text{Eq. 7}$$

where $n_{i,\,coh}$ (m^{-2}) is the number density of *i* molecules within each coherent domain. Assuming a very narrow orientational distribution of interfacial molecules, Eq. 7 gives that $\beta^{(2)}_{R,-CH_3} = 2.18 \times 10^{-27} m^4V^{-1}$ (or $1.86 \times 10^{-39}\ m^4V^{-1}s^{-1}$ with $\Gamma = 6.21\ cm^{-1}$). Along these lines we determined that $\beta^{(2)}_{NR,H_2O} = 1.28 \times 10^{-28} m^4V^{-1}$ (or $1.51 \times 10^{-42}\ m^4V^{-1}s^{-1}$ with $\Delta\omega = 450\ cm^{-1}$). Here we used $n_{-CH_3,\,coh} = 2.23 \times 10^3 m^{-2}$ and $n_{H_2O,,\,coh} = 1.18 \times 10^4\ m^{-2}$.

It is noted that our hyperpolarizability result for resonant VSFG is much lower (10^{12}) than that in the literature when using the same units.[53] This is due to the consideration of coherent domains discussed above. With the molecular hyperpolarizabilities for the resonant and nonresonant systems now known, we can consider the differences in experimental geometries for SFG and SFS systems using a common factor. That is, since the hyperpolarizability is a molecular property, we can then combine it with the number of molecules present and the appropriate geometry to quantitatively compare planar and aerosol systems.

As described above, our SFS experiments from airborne droplet exchange the planar air/liquid interface for the surfaces of submicron aerosol droplets in nitrogen. Along these lines, instead of an irradiated area on a planar surface, our SFS experiments result in a volume of irradiated particles within the aerosol stream. Specifically, the focused and overlapped 1030 nm and IR beams at the sample form a volume with the shape of two truncated cones with length equal to the Rayleigh length of the IR beam, l_R, forming the so-called Rayleigh volume, $1.61 \times 10^{-11}\ m^3$(See SI). For our particle density of $3.9 \times 10^{13}\ m^{-3}$ (Figure S10), this results in 627 droplets being irradiated in the volume. Theoretically, particles that are sufficiently small and dilute such that their surface area is less that λ^2 and the interparticle distance is much larger than their diameter, the surface of each droplet can be considered as an individual coherent domain. Our aerosol size and density fits these constrains, and the linear proportionality of our SFS signal to the aerosol density corroborate that each droplet can be considered as its own coherent domain.[17, 27, 54] In other words, $N_{coh} = N_P$. To assess the relationship between the resonant and nonresonant responses in the SFS geometry, we should be able to simply perform the above steps in reverse.

Knowing the values of $\beta^{(2)}_{R,-CH_3}$ and $\beta^{(2)}_{NR,H_2O}$ as determined from the planar surface above, we can determine susceptibilities of a single aerosol particle. With an average particle diameter of 100 nm, we calculated second-order susceptibilities for both resonant and nonresonant systems for a single particle: $\chi^{(2)}_{i,sp} = n_{i,\,SP}\langle\beta^{(2)}_i\rangle$, with $\left|\chi^{(2)}_{R,-CH_3,SP}\right| = 5.15 \times 10^{-23}\ m^2\ V^{-1}$ and $\left|\chi^{(2)}_{NR,H_2O,SP}\right| = 1.60 \times 10^{-23}\ m^2\ V^{-1}$.

Following the same procedure for the planar system, we used values of $n_{-CH_3,\,SP} = 2.36 \times 10^4\ \mathrm{m}^{-2}$ and $n_{\mathrm{H_2O},\,SP} = 1.25 \times 10^5\ \mathrm{m}^{-2}$. Since the local field factors are of relatively small consequence and are the same for the resonant and nonresonant systems, we do not include them in the determination of the effective susceptibility of a single particle, as we are only concerned with the values relative to each other. Thus, we obtained that $\left|\chi^{(2)}_{eff,i,SP}\right| = \left|\chi^{(2)}_{i,SP}\right|$. We then obtain $\left|\chi^{(2)}_{eff,-CH_3,R,SP}\right| = 5.15 \times 10^{-23}\ \mathrm{m^2\ V^{-1}}$ and $\left|\chi^{(2)}_{eff,NR,\mathrm{H_2O},SP}\right| = 1.60 \times 10^{-23}\ \mathrm{m^2\ V^{-1}}$. Thus, we have used $\beta^{(2)}_i$ from the planar solution to obtain a $\left|\chi^{(2)}_{eff,-CH_3,SP}\right| : \left|\chi^{(2)}_{eff,\mathrm{H_2O},SP}\right|$ ratio of 3.2:1, which follows the same ratio for $\left|\chi^{(2)}_{eff,\ R,-\mathrm{CH_3}}\right| : \left|\chi^{(2)}_{eff,\mathrm{H_2O},NR}\right|$ determined from the VSFG experiments above. Most importantly, this is comparable to $\left|\chi^{(2)}_{R,VSFS}\right| : \left|\chi^{(2)}_{NR,VSFS}\right| = 3.95{:}\,1$ determined from the VSFS delay data, a difference of less than 25%.

Since the VSFS signal from individual aerosols is additive, it is proportional to the number of particles, N_p, as discussed above. Thus, we can estimate the total susceptibility for all irradiated particles such that $\left|\chi^{(2)}_{eff,-CH_3,R,SFS}\right| = \sqrt{N_p}\left|\chi^{(2)}_{eff,-CH_3,R,SP}\right| = 1.29 \times 10^{-21}\ \mathrm{m^2\ V^{-1}}$ and $\left|\chi^{(2)}_{eff,NR,\mathrm{H_2O},SFS}\right| = \sqrt{N_p}\left|\chi^{(2)}_{eff,NR,\mathrm{H_2O},SP}\right| = 4.02 \times 10^{-22}\ \mathrm{m^2\ V^{-1}}$. It is noted that while these values are larger than $\left|\chi^{(2)}_{eff,\ R,-\mathrm{CH_3}}\right|$ and $\left|\chi^{(2)}_{eff,\mathrm{H_2O},NR}\right|$, respectively, but this does not necessarily mean that the observed signal from aerosol particles will be greater than the planar analog. First, the geometric difference between the planar coherent areas and aerosol particle surfaces results in over 10-times more molecules being excited in the case of airborne droplets. Another fundamental difference between the systems is the scattered nature of the SFS intensity resulting in an omnidirectional scattering pattern, whereas Eq. 1 represents a reflection geometry SFG experiment in which nearly all the generated signal is collected. However, the SF scattering pattern from airborne droplets has not yet been mapped experimentally. By these metrics, we believe that this analysis is appropriate.

Can low-repetition VSFS be performed?

Table 1. Experimental parameters for the consideration of low-repetition VSFS.

	R (kHz)	*λ* (nm)	*P* (mW)	*E* (μJ)	*τ* (fs)	*D* (***μ***m)	*I* (GW cm^{-2})	N_p	Integrated Counts
This work $VSFS_{CH3CN}$	100	1026.2	600	6.00	2360	93	37.4	627	6100
		3388	230	2.30	141	74	297		
Marchioro et al. 2022	1	800	10	10	1226	340	2.25	57200	31
		3400	10	10	120	340	27.5		
Modern 1 kHz	1	800	20	20	2000	200	31.8	5420	970
		3400	20	20	100	200	637		

Based on Eq. 2, a lower repetition rate VSF will decrease the observable signal. In this section, we will discuss the possibility of conducting VSFS experiments using an often-used and commercially available 1 kHz, 800 nm fundamental laser. In our recent response[34] to claims that our observed VSFS signal was impossible,[33] we used the point of low repetition rate and low incident fluence to show that the comparison of the two systems was invalid. In this work, an 800 nm 1 kHz pulse was used as an example. In this section we will substitute these experimental parameters into our analysis of the SFS signal, as well as parameters

from a modern 1 kHz laser system with higher power, to quantify their feasibility for conducting low-repetition VSFS experiments form airborne droplets. All parameters for this comparison as well as those used in the 100 kHz experiments are shown in Table 1.

The collected SF intensity is proportional to the product of the incident intensities, the number of irradiated particles, the repetition rate, and spectral collection time. Assuming all other values in Eq. 1 are the same across the 3 systems discussed here, we obtain that

$$I_{\mathrm{SF}}(\omega) \propto I(\omega_{\mathrm{vis}})I(\omega_{\mathrm{IR}})N_p(\omega_{\mathrm{IR}})RT. \quad \text{Eq. 8}$$

Using the 100 kHz conditions described above, we obtained an integrated VSFS intensity of about 6100 counts in 60 s, as shown in Figure 3(A). However, using the parameters from Table S9 with 60 s acquisition, the estimated intensity is nearly 50-times weaker for the previous 1 kHz system and about 6-times weaker for the modern 1 kHz system. The 1 kHz system from the literature has much lower incident intensities given the combination of low pulse energy and large spot size. While the increased spot size lets the user irradiate more particles at a time, it reduces incident intensity and makes it more difficult to focus the signal into the slit of a spectrometer and maintain spectral resolution without blocking the signal. On the other hand, the modern system has a more reasonable intensity, which can likely be overcome by increasing spectral acquisition time to 5-10 minutes. Additionally, other parameters could be optimized to enhance the possibility of observing the signal from airborne particles, such as reduced IR spot size and increased incident IR energy from simplifying the optical path. Higher incident 800 nm energy can also be used if the spot size is increased. It is important to note that a time delay between the two incident pulses will be required to remove the nonresonant/incoherent background resonant signals, which will also reduce the spectral intensity. Furthermore, the VSFS signal under the HHH polarization is nearly 20x stronger than the VVH polarization (Figure 2(A) and Figure S3(C)). Using this polarization combination may also assist others in observing VSFS signals from aerosol particles. Altogether, we believe that with modern instrumentation and care, VSFS can be powered by a 1 kHz, 800 nm laser system.

Summary and Outlook

We have provided a comprehensive analysis of the recently developed aerosol VSFS spectrometer. Through this process we have broken down the VSFS signal into coherent and incoherent as well as resonant and nonresonant components as a function of incident pulse delay time, providing valuable insights into conducting these nuanced experiments efficiently. Both VSFS and VSFG experiments were quantitatively compared using the same laser and detection systems. We extracted second-order susceptibilities and hyperpolarizabilities from resonant and nonresonant VSFG experiments and used them to determine sing-particle susceptibilities which align with the resonant/nonresonant data determined by studying the VSFS time profile. A quantitative analysis of the planar and scattering detection systems was performed, which allowed us to calculate conversion efficiencies for our VSFG, VSFS, and other nonlinear scattering experiments. Additionally, the system of aerosol VSFS does not yet have a well-understood reference material, but the incoherent SFS signal from water droplets may be a convenient and viable option after further characterization. Lastly, the potential of a 1 kHz VSFS system was discussed where it was considered plausible but ultimately less efficient than a 100 kHz system. Altogether, VSFS from airborne droplets has been shown to follow the same fundamental guidelines of VSFG from the air/liquid interface and through this work has been made more accessible to other researchers who with unique and interesting horizons.

Future works in VSFS and nonlinear optical scattering techniques hinge on robust theories and experiments which are well-aligned. However, crucial experiments outlining size- and angle-dependent scattering patterns have yet to be conducted for airborne droplets due to the weak signal intensity. Currently, the experimental configuration only collects a 60° section of the scattered light. Attempts to conduct angle-

resolved experiments result in drastically reduced SFS intensities to obtain meaningful angular resolution, notably worsened by separating the horizontal and vertical scattering axes. An option to increase this signal level is to increase the slit width on the spectrometer, but this sacrifices spectral resolution. While the present work solidifies the possibility of SFS from airborne submicron droplets, their size distribution is very broad and does not contribute significantly to the study of size-dependent SFS. To conduct size-dependent SFS experiments, droplets or particles of a narrow size range must be selected to study their nonlinear optical properties. However, instruments to complete this size classification have very low throughput efficiencies rendering the SFS intensity too weak to measure. Therefore, to conduct well-planned size- and angle- resolved experiments, innovative methods for increasing the SFS intensity must be pursued beyond increasing incident power and detection efficiency.

Supporting Information

Additional experimental details, time delay sum-frequency data, polarized VSFS data, additional calculations for normalization and signal estimation, aerosol particle size and accompanying calculations, experimental efficiencies, incoherent SFS as a standard, and feasibility of VSFS at 1 kHz, I.

Notes

The authors declare no competing financial interests.

Authors Contributions

*Corresponding author: yi.rao@usu.edu

Acknowledgements

This material is based upon work supported by the National Science Foundation under Grant No. [2203983].

References

(1) Yan, X.; Bain, R. M.; Cooks, R. G. Organic Reactions in Microdroplets: Reaction Acceleration Revealed by Mass Spectrometry. *Angew. Chem. Int. Ed.* **2016**, *55* (42), 12960-12972. DOI: 10.1002/anie.201602270.
(2) Tran Huu, H.; Vu, N. H.; Ha, H.; Moon, J.; Kim, H. Y.; Im, W. B. Sub-micro droplet reactors for green synthesis of Li3VO4 anode materials in lithium ion batteries. *Nat. Commun.* **2021**, *12* (1), 3081. DOI: 10.1038/s41467-021-23366-8.
(3) Ju, Y.; Zhang, H.; Wang, W.; Liu, Q.; Yu, K.; Kan, G.; Liu, L.; Jiang, J. Aqueous-Microdroplet-Driven Abiotic Synthesis of Ribonucleotides. *J. Phys. Chem. Lett.* **2022**, *13* (2), 567-573. DOI: 10.1021/acs.jpclett.1c03486.
(4) Geiger, F. M.; McNeill, V. F.; Orr-Ewing, A. J. Virtual Issue on Atmospheric Aerosol Research. *J. Phys. Chem. A* **2022**, *126* (32), 5233-5235. DOI: 10.1021/acs.jpca.2c04827.
(5) Wokosin, K. A.; Schell, E. L.; Faust, J. A. Surfactants, Films, and Coatings on Atmospheric Aerosol Particles: A Review. *Environ. Sci.: Atmos.* **2022**, *2*, 775-828. DOI: 10.1039/D2EA00003B.
(6) Lim, C. Y.; Browne, E. C.; Sugrue, R. A.; Kroll, J. H. Rapid heterogeneous oxidation of organic coatings on submicron aerosols. *Geophys. Res. Lett.* **2017**, *44* (6), 2949-2957. DOI: 10.1002/2017GL072585.
(7) Chim, M. M.; Lim, C. Y.; Kroll, J. H.; Chan, M. N. Evolution in the Reactivity of Citric Acid toward Heterogeneous Oxidation by Gas-Phase OH Radicals. *ACS Earth Space Chem.* **2018**, *2* (12), 1323-1329. DOI: 10.1021/acsearthspacechem.8b00118.
(8) Arata, C.; Heine, N.; Wang, N.; Misztal, P. K.; Wargocki, P.; Bekö, G.; Williams, J.; Nazaroff, W. W.; Wilson, K. R.; Goldstein, A. H. Heterogeneous Ozonolysis of Squalene: Gas-Phase Products Depend on Water Vapor Concentration. *Environ. Sci. Technol.* **2019**, *53* (24), 14441-14448. DOI: 10.1021/acs.est.9b05957.

(9) Rovelli, G.; Jacobs, M. I.; Willis, M. D.; Rapf, R. J.; Prophet, A. M.; Wilson, K. R. A critical analysis of electrospray techniques for the determination of accelerated rates and mechanisms of chemical reactions in droplets. *Chem. Sci.* **2020**, *11* (48), 13026-13043.
(10) Corral Arroyo, P.; David, G.; Alpert, P. A.; Parmentier, E. A.; Ammann, M.; Signorell, R. Amplification of light within aerosol particles accelerates in-particle photochemistry. *Science* **2022**, *376* (6590), 293-296. DOI: doi:10.1126/science.abm7915.
(11) Marcolli, C.; Krieger, U. K. Relevance of Particle Morphology for Atmospheric Aerosol Processing. *Trends Chem.* **2020**, *2* (1), 1-3. DOI: 10.1016/j.trechm.2019.11.008.
(12) McNeill, V. F. Aqueous Organic Chemistry in the Atmosphere: Sources and Chemical Processing of Organic Aerosols. *Environ. Sci. Technol.* **2015**, *49* (3), 1237-1244. DOI: 10.1021/es5043707.
(13) Renard, P.; Reed Harris, A. E.; Rapf, R. J.; Ravier, S.; Demelas, C.; Coulomb, B.; Quivet, E.; Vaida, V.; Monod, A. Aqueous Phase Oligomerization of Methyl Vinyl Ketone by Atmospheric Radical Reactions. *J. Phys. Chem. C* **2014**, *118* (50), 29421-29430. DOI: 10.1021/jp5065598.
(14) Brown, J. B.; Qian, Y.; Huang-Fu, Z.-C.; Zhang, T.; Wang, H.; Rao, Y. In Situ Probing of the Surface Properties of Droplets in the Air. *Langmuir* **2023**, *39* (31), 10724-10743. DOI: 10.1021/acs.langmuir.3c00875.
(15) Shen, Y. R. *Fundamentals of Sum-Frequency Spectroscopy*; Cambridge University Press, 2016.
(16) Zhu, X. D.; Suhr, H.; Shen, Y. R. Surface vibrational spectroscopy by infrared-visible sum frequency generation. *Phys. Rev. B* **1987**, *35* (6), 3047-3050. DOI: 10.1103/PhysRevB.35.3047.
(17) Wang, H.; Yan, E. C. Y.; Borguet, E.; Eisenthal, K. B. Second harmonic generation from the surface of centrosymmetric particles in bulk solution. *Chem. Phys. Lett.* **1996**, *259* (1), 15-20. DOI: 10.1016/0009-2614(96)00707-5.
(18) Roke, S.; Roeterdink, W. G.; Wijnhoven, J. E. G. J.; Petukhov, A. V.; Kleyn, A. W.; Bonn, M. Vibrational Sum Frequency Scattering from a Submicron Suspension. *Phys. Rev. Lett.* **2003**, *91* (25), 258302. DOI: 10.1103/PhysRevLett.91.258302.
(19) Ma, G.; Allen, H. C. Diffuse Reflection Broad Bandwidth Sum Frequency Generation from Particle Surfaces. *J. Am. Chem. Soc.* **2002**, *124* (32), 9374-9375. DOI: 10.1021/ja017864k.
(20) Srivastava, A.; Eisenthal, K. B. Kinetics of molecular transport across a liposome bilayer. *Chem. Phys. Lett.* **1998**, *292* (3), 345-351. DOI: 10.1016/S0009-2614(98)00662-9.
(21) Zeng, J.; Eckenrode, Heather M.; Dounce, Susan M.; Dai, H.-L. Time-Resolved Molecular Transport across Living Cell Membranes. *Biophys. J* . **2013**, *104* (1), 139-145. DOI: 10.1016/j.bpj.2012.11.3814.
(22) Smolentsev, N.; Roke, S. Self-Assembly at Water Nanodroplet Interfaces Quantified with Nonlinear Light Scattering. *Langmuir* **2020**, *36* (31), 9317-9322. DOI: 10.1021/acs.langmuir.0c01887.
(23) de Aguiar, H. B.; de Beer, A. G. F.; Strader, M. L.; Roke, S. The Interfacial Tension of Nanoscopic Oil Droplets in Water Is Hardly Affected by SDS Surfactant. *J. Am. Chem. Soc.* **2010**, *132* (7), 2122-2123. DOI: 10.1021/ja9095158.
(24) Smit, W. J.; Smolentsev, N.; Versluis, J.; Roke, S.; Bakker, H. J. Freezing effects of oil-in-water emulsions studied by sum-frequency scattering spectroscopy. *J. Chem. Phys.* **2016**, *145* (4), 044706. DOI: 10.1063/1.4959128.
(25) Golbek, T. W.; Strunge, K.; Chatterley, A. S.; Weidner, T. Peptide Orientation at Emulsion Nanointerfaces Dramatically Different from Flat Surfaces. *J. Phys. Chem. Lett.* **2022**, *13* (46), 10858-10862. DOI: 10.1021/acs.jpclett.2c02870.
(26) Wu, Y.; Li, W.; Xu, B.; Li, X.; Wang, H.; McNeill, V. F.; Rao, Y.; Dai, H.-L. Observation of organic molecules at the aerosol surface. *J. Phys. Chem. Lett.* **2016**, *7* (12), 2294-2297.
(27) Qian, Y.; Brown, J. B.; Huang-Fu, Z.-C.; Zhang, T.; Wang, H.; Wang, S.; Dadap, J. I.; Rao, Y. In situ analysis of the bulk and surface chemical compositions of organic aerosol particles. *Commun. Chem.* **2022**, *5* (1), 58. DOI: 10.1038/s42004-022-00674-8.
(28) Qian, Y.; Brown, J. B.; Wang, H.; Huang-Fu, Z.-C.; Zhang, T.; Narouei, F. H.; McNeill, V. F.; Rao, Y. Partitioning of Formic and Acetic Acids to the Gas/Aerosol Interface. *ACS Earth Space Chem.* **2023**, *7* (4), 885-891. DOI: 10.1021/acsearthspacechem.3c00024.
(29) Qian, Y.; Brown, J. B.; Zhang, T.; Huang-Fu, Z.-C.; Rao, Y. In Situ Detection of Chemical Compositions at Nanodroplet Surfaces and In-Nanodroplet Phases. *J. Phys. Chem. A* **2022**, *126* (23), 3758-3764. DOI: 10.1021/acs.jpca.2c03346.
(30) Qian, Y.; Deng, G.-h.; Lapp, J.; Rao, Y. Interfaces of Gas–Aerosol Particles: Relative Humidity and Salt Concentration Effects. *J. Phys. Chem. A* **2019**, *123* (29), 6304-6312.
(31) Qian, Y.; Deng, G.-h.; Rao, Y. In situ chemical analysis of the gas–aerosol particle interface. *Anal. Chem.* **2018**, *90* (18), 10967-10973.
(32) Qian, Y.; Deng, G.-h.; Rao, Y. In situ spectroscopic probing of polarity and molecular configuration at aerosol particle surfaces. *J. Phys. Chem. Lett.* **2020**, *11* (16), 6763-6771.

(33) Marchioro, A.; Golbek, T. W.; Chatterley, A. S.; Weidner, T.; Roke, S. A discrepancy of 107 in experimental and theoretical density detection limits of aerosol particles by surface nonlinear light scattering. *Commun. Chem.* **2023**, *6* (1), 114. DOI: 10.1038/s42004-023-00903-8.
(34) Qian, Y.; Brown, J. B.; Huang-Fu, Z.-C.; Zhang, T.; Wang, H.; Wang, S.; Dadap, J. I.; Rao, Y. Reply to: A discrepancy of 107 in experimental and theoretical density detection limits of aerosol particles by surface nonlinear light scattering. *Commun. Chem.* **2023**, *6* (1), 115. DOI: 10.1038/s42004-023-00904-7.
(35) Lütgebaucks, C.; Gonella, G.; Roke, S. Optical label-free and model-free probe of the surface potential of nanoscale and microscopic objects in aqueous solution. *Phys. Rev. B* **2016**, *94* (19), 195410. DOI: 10.1103/PhysRevB.94.195410.
(36) Hu, X.-H.; Wei, F.; Wang, H.; Wang, H.-F. α-Quartz Crystal as Absolute Intensity and Phase Standard in Sum-Frequency Generation Vibrational Spectroscopy. *J. Phys. Chem. C* **2019**, *123* (24), 15071-15086. DOI: 10.1021/acs.jpcc.9b03202.
(37) Wei, X.; Hong, S.-C.; Zhuang, X.; Goto, T.; Shen, Y. R. Nonlinear optical studies of liquid crystal alignment on a rubbed polyvinyl alcohol surface. *Phys. Rev. E* **2000**, *62* (4), 5160-5172. DOI: 10.1103/PhysRevE.62.5160.
(38) Zhang, T.; Huangfu, Z.-C.; Qian, Y.; Lu, Z.; Gao, H.; Rao, Y. Spectral Phase Measurements of Heterodyne Detection in Interfacial Broadband Electronic Spectroscopy. *J. Phys. Chem. C* **2022**, *126* (5), 2823-2832. DOI: 10.1021/acs.jpcc.1c09692.
(39) Lagutchev, A.; Hambir, S. A.; Dlott, D. D. Nonresonant Background Suppression in Broadband Vibrational Sum-Frequency Generation Spectroscopy. *J. Phys. Chem. C* **2007**, *111* (37), 13645-13647. DOI: 10.1021/jp075391j.
(40) Stiopkin, I. V.; Jayathilake, H. D.; Weeraman, C.; Benderskii, A. V. Temporal effects on spectroscopic line shapes, resolution, and sensitivity of the broad-band sum frequency generation. *J. Chem. Phys.* **2010**, *132* (23). DOI: 10.1063/1.3432776 (acccessed 7/12/2024).
(41) Shalhout, F. Y.; Malyk, S.; Benderskii, A. V. Relative Phase Change of Nearby Resonances in Temporally Delayed Sum Frequency Spectra. *J. Phys. Chem. Lett.* **2012**, *3* (23), 3493-3497. DOI: 10.1021/jz3014437.
(42) Velarde, L.; Wang, H.-F. Unified treatment and measurement of the spectral resolution and temporal effects in frequency-resolved sum-frequency generation vibrational spectroscopy (SFG-VS). *Phys. Chem. Chem. Phys.* **2013**, *15* (46), 19970-19984, 10.1039/C3CP52577E. DOI: 10.1039/C3CP52577E.
(43) Kim, J.; Chou, K. C.; Somorjai, G. A. Structure and Dynamics of Acetonitrile at the Air/Liquid Interface of Binary Solutions Studied by Infrared−Visible Sum Frequency Generation. *J. Phys. Chem. B* **2003**, *107* (7), 1592-1596. DOI: 10.1021/jp021227e.
(44) Zhang, D.; Gutow, J.; Eisenthal, K.; Heinz, T. Sudden structural change at an air/binary liquid interface: Sum frequency study of the air/acetonitrile–water interface. *J. Chem. Phys.* **1993**, *98* (6), 5099-5101.
(45) Wang*, H.-F.; Gan, W.; Lu†‡ §, R.; Rao†‡¶, Y.; Wu, B.-H. Quantitative spectral and orientational analysis in surface sum frequency generation vibrational spectroscopy (SFG-VS). *Int. Rev. Phys. Chem.* **2005**, *24* (2), 191-256.
(46) Boyd, R. W. *Nonlinear Optics*; Academic Press, 2008.
(47) Shen, Y.-R. *The Principles of Nonlinear Optics*; John Wiley & Sons, 1984.
(48) Marmolejos, J. M.; Bisson, P. J.; Shultz, M. J. Gold as a standard phase reference in complex sum frequency generation measurements. *J. Chem. Phys.* **2019**, *150* (12). DOI: 10.1063/1.5081147 (acccessed 4/24/2024).
(49) Feng, R.-r.; Guo, Y.; Lü, R.; Velarde, L.; Wang, H.-f. Consistency in the Sum Frequency Generation Intensity and Phase Vibrational Spectra of the Air/Neat Water Interface. *J. Phys. Chem. A* **2011**, *115* (23), 6015-6027. DOI: 10.1021/jp110404h.
(50) Zhuang, X.; Miranda, P. B.; Kim, D.; Shen, Y. R. Mapping molecular orientation and conformation at interfaces by surface nonlinear optics. *Phys. Rev. B* **1999**, *59* (19), 12632-12640. DOI: 10.1103/PhysRevB.59.12632.
(51) Hamm, P. a. Z., Martin. *Concepts and Methods of 2D Infrared Spectroscopy*; Cambridge University Press, 2011.
(52) Shen, Y. R.; Ostroverkhov, V. Sum-Frequency Vibrational Spectroscopy on Water Interfaces: Polar Orientation of Water Molecules at Interfaces. *Chem. Rev.* **2006**, *106* (4), 1140-1154. DOI: 10.1021/cr040377d.
(53) Oh-e, M.; Lvovsky, A. I.; Wei, X.; Shen, Y. R. Sum-frequency generation (SFG) vibrational spectroscopy of side alkyl chain structures of polyimide surfaces. *J. Chem. Phys.* **2000**, *113* (19), 8827-8832. DOI: 10.1063/1.1318199 (acccessed 4/24/2024).
(54) Roke, S.; Gonella, G. Nonlinear Light Scattering and Spectroscopy of Particles and Droplets in Liquids. *Annu. Rev. Phys. Chem.* **2012**, *63* (Volume 63, 2012), 353-378. DOI: 10.1146/annurev-physchem-032511-143748.

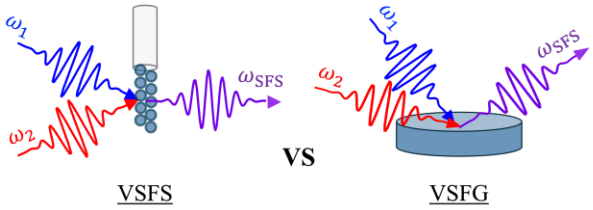
ω1
ω2
ωSFS
VS
ω1
ω2
ωSFS
VSFS
VSFG